Journal of
Applied Physics

RESEARCH ARTICLE | APRIL 22 2024

Large electrocaloric effect near room temperature induced by domain switching in ferroelectric nanocomposites

Zeqing Yu ; Xu Hou ; Sizheng Zheng ; Chengwen Bin ; Jie Wang

Check for updates

J. Appl. Phys. 135, 164105 (2024)
https://doi.org/10.1063/5.0205338

View Online
Export Citation

Articles You May Be Interested In

Near room-temperature large negative electrocaloric effect accompanied by giant thermal switching ratio in Zr-rich lead zirconate titanate

Appl. Phys. Lett. (September 2024)

Lead free $Ba_{0.8}Ca_{0.2}Te_xTi_{1-x}O_3$ ferroelectric ceramics exhibiting high electrocaloric properties

J. Appl. Phys. (February 2017)

Electrocaloric effect in pure and $NaNbO_3$-modified $Na_{0.5}Bi_{0.5}TiO_3$–$BaTiO_3$ solid solutions near the morphotropic phase boundary

J. Appl. Phys. (September 2023)

27 November 2025 08:52:18

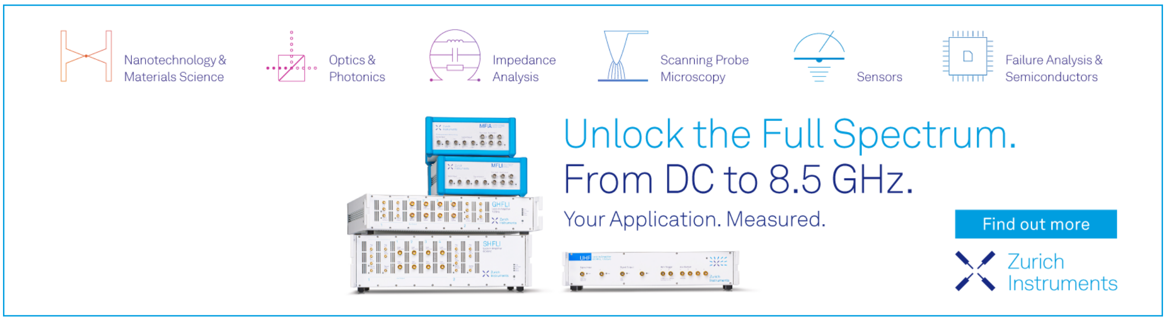
Nanotechnology & Materials Science
Optics & Photonics
Impedance Analysis
Scanning Probe Microscopy
Sensors
Failure Analysis & Semiconductors
Unlock the Full Spectrum.
From DC to 8.5 GHz.
Your Application. Measured.
Find out more
Zurich Instruments

AIP Publishing

Journal of
Applied Physics

ARTICLE

pubs.aip.org/aip/jap

Large electrocaloric effect near room temperature induced by domain switching in ferroelectric nanocomposites

Cite as: J. Appl. Phys. **135**, 164105 (2024); doi: 10.1063/5.0205338
Submitted: 26 February 2024 · Accepted: 4 April 2024 ·
Published Online: 22 April 2024

View Online Export Citation CrossMark

Zeqing Yu,[1] Xu Hou,[2] Sizheng Zheng,[1] Chengwen Bin,[1] and Jie Wang[1,3,4,a)]

AFFILIATIONS

[1] Department of Engineering Mechanics, Zhejiang University, Zheda Road 38, Hangzhou, Zhejiang 310027, China
[2] Department of Industrial and Systems Engineering, Research Institute for Advanced Manufacturing, The Hong Kong Polytechnic University, Hung Hom, Kowloon, Hong Kong, China
[3] Zhejiang Laboratory, Hangzhou, Zhejiang 311100, China
[4] Key Laboratory of Soft Machines and Smart Devices of Zhejiang Province, Zhejiang University, Zheda Road 38, Hangzhou, Zhejiang 310027, China

[a)] **Author to whom correspondence should be addressed:** jw@zju.edu.cn

27 November 2025 08:52:18

ABSTRACT

The solid-state refrigeration technique based on the electrocaloric effect (ECE) of ferroelectric materials has been regarded as a promising alternative to vapor compression systems due to its advantages of high efficiency and easy miniaturization. However, the small adiabatic temperature change (ATC) and narrow operating temperature range of ferroelectric materials are key obstacles for their practical applications of ECE refrigeration. To improve the ECE performance of ferroelectric polymer poly(vinylidene fluoride) [P(VDF-TrFE)], $PbZr_{1-x}Ti_xO_3$ (PZT) nanoparticles with larger polarization is herein introduced to form ferroelectric nanocomposites. The phase-field simulation is employed to investigate the dynamic hysteresis loops and corresponding domain evolution of the ferroelectric nanocomposites. The temperature-dependent ATC values are calculated using the indirect method based on the Maxwell relation. The appearance of the double hysteresis loop is observed in P(VDF-TrFE) nanocomposite filled with $PbZr_{0.1}Ti_{0.9}O_3$ nanoparticles [P(VDF-TrFE)–$PZT_{0.9}$], which is mainly caused by a microscopic domain transition from single domain to polar vortex. Compared to the P(VDF-TrFE), enhanced ATC values associated with the domain transition are unveiled in P(VDF-TrFE)–$PZT_{0.9}$, and the temperature range of excellent ECE is also effectively broadened. In addition, as the component x of filled PZT nanoparticles increases to cross the morphotropic phase boundary (MPB), the maximum ATC value shows a significant increase. The results presented in this work not only explain the mechanism of domain transition induced excellent ECE in the P(VDF-TrFE)–PZT nanocomposite, but also stimulate future studies on enhancing ECE of P(VDF-TrFE) by introducing ferroelectric nanofillers.

© 2024 Author(s). All article content, except where otherwise noted, is licensed under a Creative Commons Attribution (CC BY) license (https://creativecommons.org/licenses/by/4.0/). https://doi.org/10.1063/5.0205338

I. INTRODUCTION

In industrial production and modern daily life, refrigeration technology is widely used in various fields, such as air conditioning, food freshening, and temperature management of cell phones. The traditional vapor compression cycle has dominated the market of refrigeration over a century but surfers from the problems of low energy conversion rate and environment degradation.[1] More critically, the imperative problem of thermal failure accompanied with the increasing integration of microelectronic devices seems hardly to be solved by the traditional refrigeration technology.[2] A novel solid-state cooling technology based on electrocaloric effect (ECE) technology has been demonstrated to own the advantages including environmental protection, high efficiency, easy miniaturization, low noise, etc.,[3] which exhibits significant application potential in flexible wearable refrigeration and chip cooling.[4] For this reason, the excellent ECE exhibited by ferroelectric materials has provoked researchers' enthusiasm for exploration.[5]

The ECE observed in ferroelectric materials manifests as a transition in the degree of polarization ordering in response to variations of the applied electric field. This transition consequently engenders an alteration in the adiabatic temperature change (ATC), represented by ΔT.[6–9] Near the Curie temperature T_c, ferroelectric materials undergo a phase transition from the ferroelectric phase to the paraelectric phase,[10] resulting in typically maximum value of ΔT.[11] However, the phase-transition temperature of most ferroelectric materials is much higher than room temperature, and the operating temperature zone is also very narrow,[12–14] thereby constraining their practical utility in ECE refrigeration. For example, the ferroelectric $PbZr_xTi_{1-x}O_3$ (abbreviated as PZT, where x denotes the molar fraction of dopant elements) owns a large polarization and excellent ECE,[15] but its high phase-transition temperature limits its practical application. To overcome the disadvantages of these inorganic ferroelectrics, researchers try to improve the ECE by applying external stress[16] and misfit strain,[17] or introducing defects.[18] Meanwhile, although the T_c of ferroelectric polymers such as poly(vinylidene fluoride) [P(VDF-TrFE)] is close to room temperature,[19] the potential of its ECE has not been fully exploited due to its small polarization. A composite strategy combining ferroelectric polymer matrices with low transition temperature and ceramic nanoparticles with high polarization is naturally comes to our mind,[20–23] because the overall polarization could be enhanced by constructing ferroelectric nanocomposites and improved ECE performance are expected to be achieved.[23] It has been shown that the shape,[22] composition,[24] and arrangement[25] of the nanofiller particles can have a significant impact on the ECE of ferroelectric nanocomposites.

In addition to the inherent phase transition, the domain evolution of ferroelectric also plays an important role in tuning its microscopic physical properties. Especially in nanoscale ferroelectric materials, the ECE is closely linked to the dynamic evolution of the microscopic domain structure inside the materials.[26–28] The transition from the multi-domain to mono-domain driven by temperature is corroborated to amplify the ECE of bulk $PbTiO_3$ (PTO), especially near the location of domain wall. Meanwhile, similar to the phase-transition temperature, the domain transition temperature could also be effectively adjusted by external strains.[26] Mechanical compression is employed to induce two types of pseudo-first-order phase transition in $BaTiO_3$ (BTO) nanoparticles, which could occur at a temperature below the Curie temperature and contribute to the positive and negative ECE response.[29] The influence of the surface polarization effect on the ECE of PTO nanocylinders is studied by incorporating the extrapolation length into the phase-field model. The extrapolation length possesses the capacity to modify the peak value of ΔT and shift its temperature position.[30] As shown in aforementioned three examples, the phase-field approach based on the time-dependent Ginzburg–Landau equation is effective for studying the ECE in ferroelectric materials. This approach adeptly models the intricate influence of the applied electric field and temperature on the formation and alteration of microscopic domains within ferroelectric nanostructures, which should be equally applicable for the investigation of ferroelectric nanocomposites.[31] However, the evolution of polarization within ferroelectric polymers has been largely overlooked. Additionally, the current thermodynamic theory of ferroelectric polymers lacks an electromechanical coupling term, rendering it incapable of describing the electromechanical coupling effect between the ferroelectric polymer matrix and inorganic nanofillers. Whereas, experimental observations have demonstrated that the existing of complex topological domain structure in P(VDF-TrFE), which can be even appropriately manipulated in response to the applied electric field and strain.[32,33] Therefore, it should be essential to consider the spontaneous polarization and the correlation between spontaneous polarization and strain in the P(VDF-TrFE) matrix as modeling the ferroelectric nanocomposites. Furthermore, the impact of doping elemental components of the nanofiller particles on the ECE in ferroelectric nanocomposites has not been sufficiently explored through phase-field simulations.

In this work, the ferroelectric polymer P(VDF-TrFE) (50/50 mol. %) with low transition temperature is selected as the matrix, and the ferroelectric PZT with significant polarization is used as the nanofiller particles to construct the ferroelectric nanocomposite. A transition layer between the polymer and nanoparticle is involved to consider the interfacial effect.[34] The polarization dynamic characteristics and domain structure evolution of the ferroelectric nanocomposites at the microscopic level are investigated via phase-field simulation, and the ECE performance is calculated from the indirect method based on the Maxwell relationship. By adjusting the component x, we aim to achieve precise regulation of the phase-transition properties and the domain structure of ferroelectric nanocomposites, so as to optimize the ECE of ferroelectric materials. The results presented in this work not only opens up new avenues for the application of ferroelectric nanocomposites in the fields such as energy storage and refrigeration but also provides profound insights into understanding the physical behavior of ferroelectric materials at the nanoscale.

27 November 2025 08:52:18

II. SIMULATION METHOLOGY

A. Phase-field model of ferroelectric nanocomposites

The 2D phase-field model is adopted here to investigate the ECE of ferroelectric nanocomposites. The model contains five degrees of freedom, including the displacements u_1 and u_2, the polarization components P_1 and P_2, and the electric potential φ. The free energy density f of the ferroelectric nanocomposites can be divided in to five parts: Landau, gradient of polarization, elastic, electromechanical coupling and electrostatic, expressed as follows:

$$f = f_{\mathrm{Land}} + f_{\mathrm{grad}} + f_{\mathrm{elas}} + f_{\mathrm{coup}} + f_{\mathrm{elec}}. \tag{1}$$

The Landau energy density is expanded as follows:

$$\begin{aligned} f_{\mathrm{Land}} = {} & \alpha_1((P_1)^2 + (P_2)^2) + \alpha_{11}((P_1)^4 + (P_2)^4) + \alpha_{12}(P_1)^2(P_2)^2 \\ & + \alpha_{111}((P_1)^6 + (P_2)^6) + \alpha_{112}((P_1)^2(P_2)^4 + (P_1)^4(P_2)^2). \end{aligned} \tag{2}$$

Here, α_1 represents the dielectric coefficient, defined as $(T - T_c)/(2\varepsilon_0 C_0)$. T and T_c stand for the current and Curie temperatures of the material, respectively. ε_0 and C_0 denote the vacuum dielectric constant and the Curie constant, respectively. α_{11}, α_{12}, α_{111}, and α_{112} are the higher order Landau energy coefficients.

Due to the difference in polarization orientation between different domains, a large energy is accumulated at domain wall. This phenomenon can be well described by introducing the gradient

© Author(s) 2024

energy density, expressed as

$$f_{\mathrm{grad}} = \frac{1}{2}G_{11}((P_{1,1})^2 + (P_{2,2})^2) + G_{12}P_{1,1}P_{2,2} + \frac{1}{2}G_{44}(P_{1,2} + P_{2,1})^2 + \frac{1}{2}G'_{44}(P_{1,2} - P_{2,1})^2, \quad (3)$$

where G_{11}, G_{12}, G_{44}, and G'_{44} are the polarization gradient energy coefficients and $P_{i,j}(i,\ j = 1, 2)$ are the derivative of the polarization component P_i with respect to the coordinate x_j. The third term in Eq. (1) is elastic energy density, expanded as

$$f_{\mathrm{elas}} = \frac{1}{2}c_{11}((\varepsilon_{11})^2 + (\varepsilon_{22})^2) + c_{12}\varepsilon_{11}\varepsilon_{22} + 2c_{44}(\varepsilon_{12})^2, \quad (4)$$

where c_{11}, c_{12}, and c_{44} are the elastic coefficients and $\varepsilon_{ij}(i,\ j = 1, 2)$ are the components of total strain. The strain-dependent electrostrictive energy density is shown below

$$f_{\mathrm{coup}} = -q_{11}(\varepsilon_{11}(P_1)^2 + \varepsilon_{22}(P_2)^2) - q_{12}(\varepsilon_{11}(P_2)^2 + \varepsilon_{22}(P_1)^2), \quad (5)$$

where q_{11} and q_{12} are the electrostriction coefficients. The electric field energy density is obtained using the Legendre transform, wrote as

$$f_{\mathrm{elec}} = -\frac{1}{2}\kappa_c\varepsilon_0((E_1)^2 + (E_2)^2) - (E_1P_1 + E_2P_2), \quad (6)$$

where ε_0 is the vacuum dielectric constant, κ_c is the background dielectric coefficient of the material, and E_1 and E_2 are the electric field components.

The time-dependent Ginzburg–Landau (TDGL) equation is used to describe the evolution of the polarization, expressed as

$$\frac{\partial P_i(\boldsymbol{r}, t)}{\partial t} = -L\frac{\delta F}{\delta P_i(\boldsymbol{r}, t)}(\mathrm{i} = 1, 2), \quad (7)$$

where $\boldsymbol{r} = (x_1, x_2)$ is the spatial position vector, t denotes the time, L is the kinetic coefficient, and $F = \int_{\mathrm{v}} f dV$ is the total free energy of the ferroelectric nanocomposite. $\delta F/\delta P_i(\boldsymbol{r}, t)$ denotes the driving force for the evolution of the polarization in thermodynamics. The mechanical equilibrium equation assumes the following form:

$$\frac{\partial}{\partial x_j}\left(\frac{\partial f}{\partial \varepsilon_{ij}}\right) = 0. \quad (8)$$

Maxwell's equation is given as

$$\frac{\partial}{\partial x_i}\left(-\frac{\partial f}{\partial E_i}\right) = 0. \quad (9)$$

To address the partial differential equation at hand, a multi-field coupling nonlinear finite element method is utilized. The detailed implementation process can be found in the previous work.[35]

To simulate the interested area of ferroelectric materials, a representative cell with the size of $50 \times 100\,\mathrm{nm}^2$ was selected, as illustrated in Fig. 1. The model features a short circuit condition for the top and bottom boundaries to describe their contacting with electrodes. Additionally, periodic boundary conditions for displacements, electric potential, and polarization components are employed along the X_1 direction. Furthermore, the rigid body displacements are excluded. In the model shown in Fig. 1(a), the blue region represents P(VDF-TrFE), which is characterized by a low T_c that is close to room temperature. The PZT nanoparticles, which are noted for their large spontaneous polarization P_s, are depicted by the pink region in Fig. 1(b). To specifically investigate the effect of filled nanoparticles on the ECE, PZT nanoparticles with different component x were added to the P(VDF-TrFE) matrix to constitute a novel ferroelectric nanocomposite [P(VDF-TrFE)–PZT$_x$], as demonstrated in Fig. 1(c). The ratio of the matrix to nanoparticles by volume is consistently maintained at 70:30.

In the considered ferroelectric nanocomposites, the introduction of filled PZT nanoparticles not only provides a large polarization but also introduces new interfacial effects. It has been elucidated that the nature of the interface between the nanoparticles and the matrix has a strong impact on the properties of the composites.[36,37] The rational design of interfacial effects[38] is an effective strategy to optimize the properties of materials. To achieve a closer approximation of the experimental data, the interfacial layer [i.e., the yellow area in Fig. 1(c)] is incorporated into the model. The thickness of the boundary layer is set to 12% of the radius of the filled particles.[34] Spatially dependent material coefficients are employed to encapsulate the heterogeneity between the different regions of P(VDF-TrFE), PZT, and the interfacial layer. Consequently, the Landau energy coefficients for the interfacial layer are assigned as the mean values of those for P(VDF-TrFE) and PZT. Other material parameters, such as the elastic constants of the interfacial layer, are selected based on the properties of P(VDF-TrFE). The Landau energy coefficients of P(VDF-TrFE) are obtained from empirical fitting. First, α_0 is obtained from the temperature-dependent dielectric constant curves derived from the previous experiments.[39] Then, the other Landau energy coefficients is determined based on the hysteresis loops of P(VDF-TrFE)

27 November 2025 08:52:18

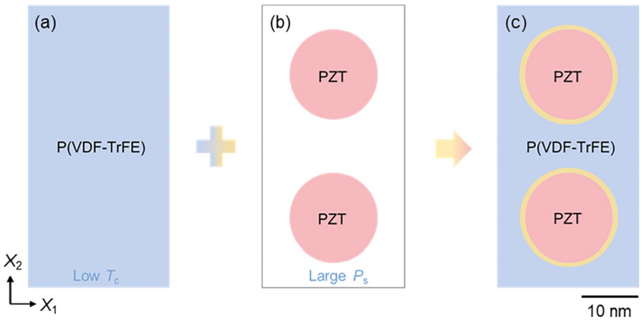

FIG. 1. The model of the ferroelectric nanocomposite, with 10 nm scale bar. Schematic of the combination of (a) P(VDF-TrFE) matrix with low T_c and (b) filled PZT nanoparticles with large saturated polarization P_s for (c) the designed ferroelectric nanocomposite. The yellow ring represents the consideration of interface layer between the P(VDF-TrFE) matrix and filled PZT nanoparticles.

50/50 mol from the previous experiments.[40] The parameters for P(VDF-TrFE) and PZT[41] utilized are comprehensively listed in the Appendix.

The model was discretized by using four-node grids. Each node has five degrees of freedom, including two displacement components, one potential, and two polarization components. The initial value of the local polarization components in the simulated region is randomly generated, and the average polarization magnitude is kept as zero. The electric field is applied in a function of triangular wave by assigning voltage values on the bottom edge and keeping the top surface to be grounded. Sufficient simulation steps are undertaken to ensure the polarization distribution has essentially reached a steady state at a specific temperature and applied electric field. In this paper, the average value of polarization along the X_2 direction is taken as the macroscopic polarization of ferroelectric materials.

B. Calculation of ECE by the indirect method

Similar to that employed in experimental works,[42] the ATC ΔT in this paper were obtained by an indirect method based on Maxwell's relation.[43] The average polarization vs the electric field E_2 (P–E) hysteresis loops are calculated to provide original data. A maximum electric field is first applied along the $+X_2$ direction of the nanocomposite model to reach a single domain state. After that, the electric field is sequentially reduced to zero and then increased at equal intervals along the $-X_2$ direction until it reaches the maximum value. The maximum applied electric field is set to be 100 MV/m, which is below the breakdown field strength but above the saturation field of the ferroelectric nanocomposites. The increase and decrease of the electric field are carried out at intervals of the magnitude of 0.2 MV/m.

Based on the P–E loops of the nanocomposite models at different temperatures, the polarization vs temperature P–T curves at different electric fields can be obtained. The slope of two adjacent temperature points is used as the dP/dT value corresponding to the central temperature. The specific expression[44–46] for the ATC ΔT can be then calculated using the following formula:

$$\Delta T = -\int_{E_a}^{E_b} \frac{T}{C_\rho}\left(\frac{\partial P_i}{\partial T}\right)_{E_i} dE_i, \tag{10}$$

where C_ρ is expressed as the heat capacity per unit volume of the material and can be obtained based on the average volume ratio of P(VDF-TrFE) and PZT. The C_ρ of P(VDF-TrFE)[47] is approximated to be 2.52×10^6 J/K m^3. The C_ρ of PZT[45] is approximated to be 3.00×10^6 J/K m^3. According to geometric configuration, the percentage of P(VDF-TrFE) is 0.7 and that of PZT is 0.3, which gives $C_\rho = 2.664 \times 10^6$ J/K m^3 for the ferroelectric nanocomposites in this paper. According to Eq. (10), it is not difficult to notice that the ATC ΔT possesses not only a proportional relationship with $(dP/dT)_E$, but also a close dependence of the changing limits of the electric field. The discrete integration of the curve of dP/dT vs E can be used to figure out the ΔT corresponding to each temperature. Eventually, the ΔT–T curves of each ferroelectric model under different electric fields can be plotted.

III. RESULTS AND DISCUSSION

A. Evaluation of the ECE of P(VDF-TrFE)

The Landau expansion coefficients utilized in this work are meticulously calibrated to the experimental measurements, ensuring an accurate prediction of the ECE of P(VDF-TrFE) at a 50/50 mol. % ratio. To evaluate the reliability of these coefficients, several P–E hysteresis loops of single domain P(VDF-TrFE) are calculated across a temperature spectrum ranging from 21 to 93 °C, with increments of 8 °C. Only four representative P–E loops at temperatures of 21, 45, 69, and 93 °C are illustrated in Fig. 2(a). At 21 °C, the coercive field E_c of P(VDF-TrFE) is 73.1 MV/m, consistent with experimental measurements,[48] and the P–E loop exhibits a relatively regular pattern. With increasing temperature, the coercive field decreases, leading to a reduction in the enclosed area of the entire P–E loop. Once the temperature exceeds the T_c of 59.26 °C, a phase transition occurs, causing P(VDF-TrFE) to become paraelectric, thereby eliminating the hysteresis observed in the P–E loop.

By transforming the P–E loops at various temperatures, the polarization–temperature (P–T) curves under different electric fields can be obtained. Similarly, only seven representative P–T curves under varying electric fields are selected for comparative analysis, as shown in Fig. 2(b). An increase in the electric field results in an upward shift of the P–T curves, indicating a rise in the average polarization values of P(VDF-TrFE). Under the same electric field, the P–T curve demonstrates a steady decline, related to a gradual decrease in average polarization with temperature increment. Particularly, a rapid drop in average polarization is observed in the temperature region between 53 and 61 °C, leading to the peak value of dP_2/dT–T curves of P(VDF-TrFE) occurring at 57 °C, as illustrated in Fig. 2(c). Subsequently, the ATC ΔT is calculated by Eq. (10), and the ΔT vs temperature T (ΔT–T) curves of P(VDF-TrFE) under different electric fields are depicted in Fig. 2(d). At a given temperature, a higher electric field corresponds to a greater ΔT for P(VDF-TrFE), and the peak ΔT always occurs at 57 °C regardless of the electric field. The hollow green square symbols in Fig. 2(d) represent the previous experimental measurements[19] of ΔT values of P(VDF-TrFE) under an electric field of 134 MV/m. It can be observed that the ΔT values of P(VDF-TrFE) obtained from the phase-field simulation at 134 MV/m closely align with the previous experimental measurements. This implies that the established electromechanical coupling phase-field model of ferroelectric polymer is effective and the Landau energy coefficients adopted in this paper are reliable.

27 November 2025 08:52:18

B. Double hysteresis loop of P(VDF-TrFE)-PZT$_{0.9}$ nanocomposite

After evaluating the ECE of P(VDF-TrFE), further simulations are conducted on the ferroelectric nanocomposites filled with nanoparticles of $PbZr_{0.1}Ti_{0.9}O_3$, denoted as P(VDF-TrFE)-PZT$_{0.9}$. In the same approach as in section A, the P–E loop of nanocomposite is first calculated. However, different from both P(VDF-TrFE) and PZT$_{0.9}$, P(VDF-TrFE)-PZT$_{0.9}$ nanocomposites exhibits a double hysteresis loop at 21 °C, as illustrated in Fig. 3(a). The prominent characteristic of the double loop is the drop in polarization, which occurs from point 2 to point 7, with the associated electric field defined as E_2^I. In a similar manner, there is a notable leap in polarization from point 8 to point 1, with this corresponding electric field designated as E_2^{II}.

© Author(s) 2024

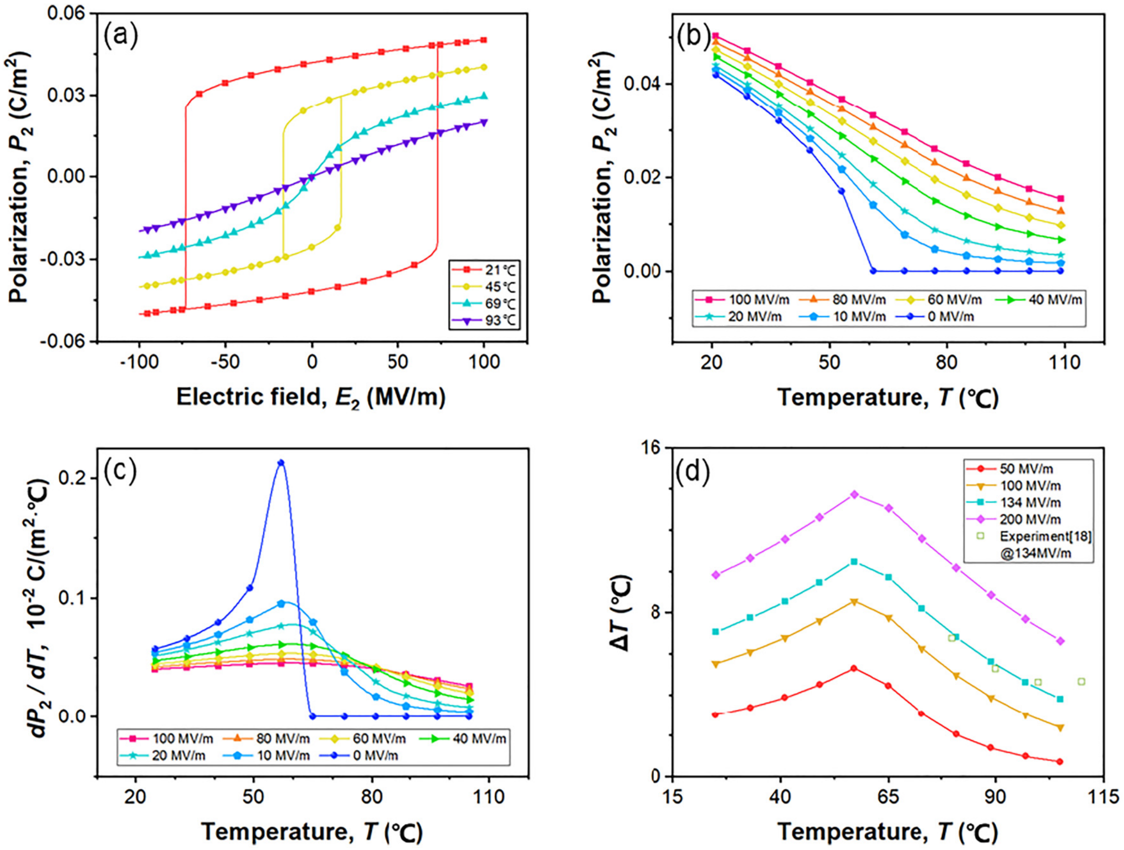

27 November 2025 08:52:18

FIG. 2. The ECE of single domain P(VDF-TrFE). (a) Hysteresis loops at different temperatures, (b) polarization P_2 vs temperature T (P–T) curves at different electric fields, (c) dP_2/dT vs temperature T (dP_2/dT–T) curves, and (d) ATC ΔT vs temperature T (ΔT–T) curves under certain electric field changes of the P(VDF-TrFE). The hollow green square symbol represents the magnitude of the ATC ΔT for P(VDF-TrFE) under 134 MV/m in the previous experimental work.[19]

The emergence of the double loop is closely related to the dynamical evolution of domain structures under varying applied electric field, as listed in Fig. 3(b) corresponding to the labeled points in Fig. 3(a). In the domain structure, the contour plot represents the actual magnitude of polarization along the X_2 direction, and the arrows indicate the magnitude and direction of the total polarization. Due to the small contribution of P(VDF-TrFE) to the average polarization, the arrows within P(VDF-TrFE) are not displayed. At the same time, the main focus here is to describe the evolution of the domain structure in PZT. As the applied electric field E_2 decreases from points 1 to 2, the polarization in the nanocomposites still points in the $+X_2$ direction, resulting in a smooth decrease in average polarization. Continue to decrease E_2 to -12 MV/m at point 3, polarization along the $-X_2$ direction is induced to be appeared near the interface of PZT nanoparticle and the P(VDF-TrFE) matrix, subsequently evolving into vortex domains in PZT. This domain transition leads to a sharply plunge of average polarization from points 2 to 3. From points 3 to 4, the positive electric field is gradually reduced to zero and then incrementally increased in the negative direction, resulting in a reduced ratio of polarization along $+X_2$ to $-X_2$. As the electric field increases along $-X_2$ from points 4 to 5, the vortex domains in the PZT nanoparticles evolve into single domains with an abrupt change in the average polarization. Subsequent variations in the applied electric field from points 5 to 8 correspond to domain structure dynamics with evolving behavior similar to that of points 1 to 4. The transition between single and vortex domains in the PZT nanoparticle-filled region also occurs around the electric fields with absolute value of E_2^I and E_2^{II}.

Not only at 21 °C, the P–E loops of P(VDF-TrFE)–PZT$_{0.9}$ nanocomposite under different temperature also exhibit the double hysteresis behavior, as demonstrated in Fig. 3(c). With the increase of temperature, all the polarization values at various electric field show a decreasing trend, and the corresponding enclosed area of the double hysteresis loop is gradually contracted. The domain evolution stages along the hysteresis loops under different temperature are similar to that at 21 °C, and the abrupt drop and leap of polarization are also related to the domain transitions between single domain and vortex domain inside PZT. It is clear to be seen from Fig. 3(c) that E_2^I exhibit a gradual increment from 12 to 27.2 MV/m with rising temperature, while E_2^{II} almost keeps in the same location.

© Author(s) 2024

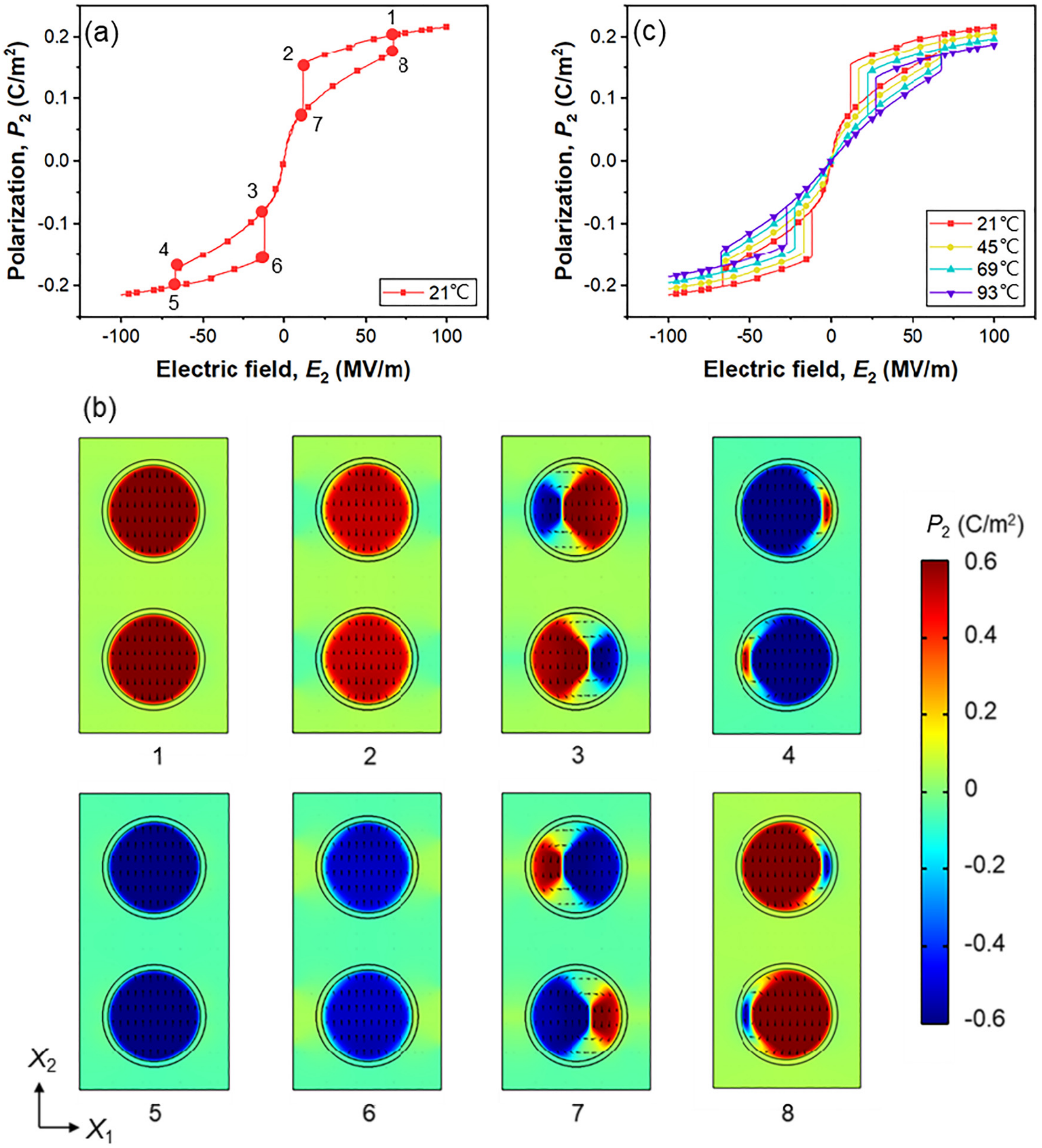

FIG. 3. Double hysteresis loops of P(VDF-TrFE)-PZT$_{0.9}$ and related domain structures. (a) The double hysteresis loop observed at 21 °C in the ferroelectric nanocomposite P(VDF-TrFE)–PZT$_{0.9}$. (b) Domain structures associated with the emergence of double returns, corresponding to the points in (a), respectively. (c) The temperature dependence of hysteresis loops.

27 November 2025 08:52:18

C. Enhanced ECE in the P(VDF-TrFE)–PZT$_{0.9}$ nanocomposite

Based on the P–E loops of the P(VDF-TrFE)–PZT$_{0.9}$ nanocomposites measured at different temperatures, we can derive the P–T curves of the nanocomposites when subject to various electric field ranging from 0 to 100 MV/m. Figure 4(a) demonstrates the specific P–T curves of the P(VDF-TrFE)–PZT$_{0.9}$ at seven selected electric field values. These curves provide insights into the temperature-dependent polarization behavior of the P(VDF-TrFE)–PZT$_{0.9}$ in the presence of an applied electric field. After the fully withdraw of electric field, the P–T curve appears relatively stable with polarization value close to zero across the temperature range. However, under an applied electric field of 10 MV/m, the P–T curve exhibits a

© Author(s) 2024

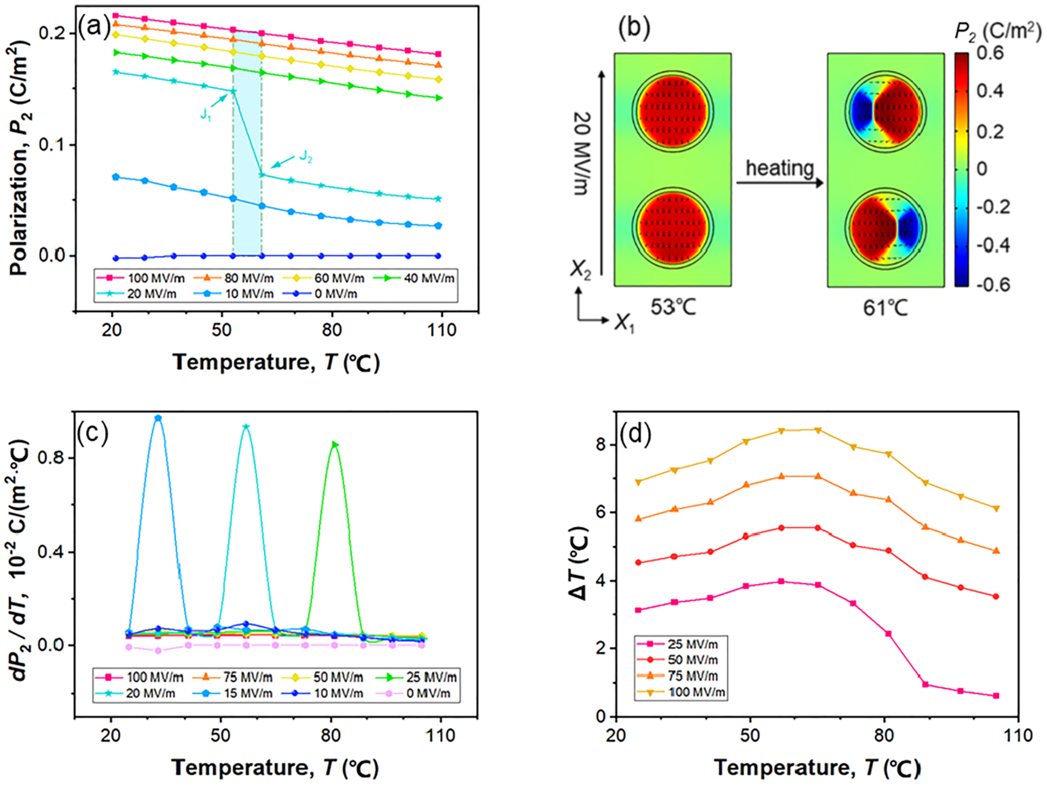

FIG. 4. Temperature-dependent polarization and ECE of P(VDF-TrFE)–PZT$_{0.9}$. (a) P–T curves at selected electric fields, (b) the domain transition behavior from J$_1$ to J$_2$ at 20 MV/m, (c) dP_2/dT–T curves at selected electric fields, and (d) ΔT–T curves under several electric field changes of P(VDF-TrFE)–PZT$_{0.9}$ nanocomposite.

27 November 2025 08:52:18

monotonously decreasing behavior as the temperature climbs. The incremental elevation of the electric field results in a continuous augmentation of the polarization value in P(VDF-TrFE)–PZT$_{0.9}$. A notable sharp plunging is observed in the P–T curves at specific electric fields such as 15, 20, and 25 MV/m. Note that similar abrupt declining trend also occurs at some other nearby electric fields which is not displayed in Fig. 4(a). To rationalize the plunge of the P–T curve, exemplified by the case of 20 MV/m, the temperature region from 53 to 61 °C is marked in blue in Fig. 4(a), and the characteristic points J$_1$ and J$_2$ near its plunge are selected for microstructure analysis. As revealed in Fig. 4(b), as the temperature ascends from 53 to 61 °C, there is a significant increase in domain walls within the PZT nanoparticle-filled regions from J$_1$ to J$_2$. The emergence of negative domains in the vortex domain leads to a rapid decrease in the overall average polarization.

Figure 4(c) shows the dP_2/dT–T curves of the P(VDF-TrFE)–PZT$_{0.9}$, which is obtained from the temperature derivation of the P–T curves. Obvious peaks are observed in the dP_2/dT–T curves at electric fields of 15, 20, and 25 MV/m, exactly corresponding to the emergence of plunging of their P–T curves. For example, the peak under 20 MV/m locates at the temperature of 57 °C. The ΔT–T curves of the P(VDF-TrFE)–PZT$_{0.9}$ are exhibited in Fig. 4(d) for electric fields of 25, 50, 75, and 100 MV/m. It is observed that under the same temperature, the ΔT is enhanced but becomes less insensitive to temperature with the intensification of the electric field. All the ΔT–T curves exhibit a maximum value (i.e., Δ$T_{\max}$) at a temperature around 57 °C for different electric field changes. Specifically, a Δ$T_{\max}$ of 5.54 °C is achieved at an electric field change of 50 MV/m, and a Δ$T_{\max}$ of 8.43 °C at 100 MV/m, for the P(VDF-TrFE)–PZT$_{0.9}$ nanocomposite.

D. Effect of component *x* on the ECE of P(VDF-TrFE)–PZT*x* nanocomposites

Phase-field simulation is then further conducted to probe deeper into the influence of component x of filled PZT nanoparticles on the ECE of P(VDF-TrFE)–PZT$_x$ nanocomposites. The simulated component x is in the range from 0.1 to 0.9 with a spacing of 0.1 between adjacent computational models. The P–E loops of ferroelectric nanocomposites with component x of 0.9, 0.7, 0.5, and 0.3 are picked out to give a clear comparison under the same temperature of 21 °C, as shown in Fig. 5(a). In contrast to the small polarization and square shape of P(VDF-TrFE), all the ferroelectric nanocomposites possess a significantly enhanced polarization and relatively slim P–E loops. As the component x keeps decreasing, the maximum polarization value reduces monotonously. Double hysteresis loops similar to that of the aforementioned P(VDF-TrFE)–PZT$_{0.9}$ are still detected before the component x reaches 0.5, but the enclosed area of the P–E loops

© Author(s) 2024

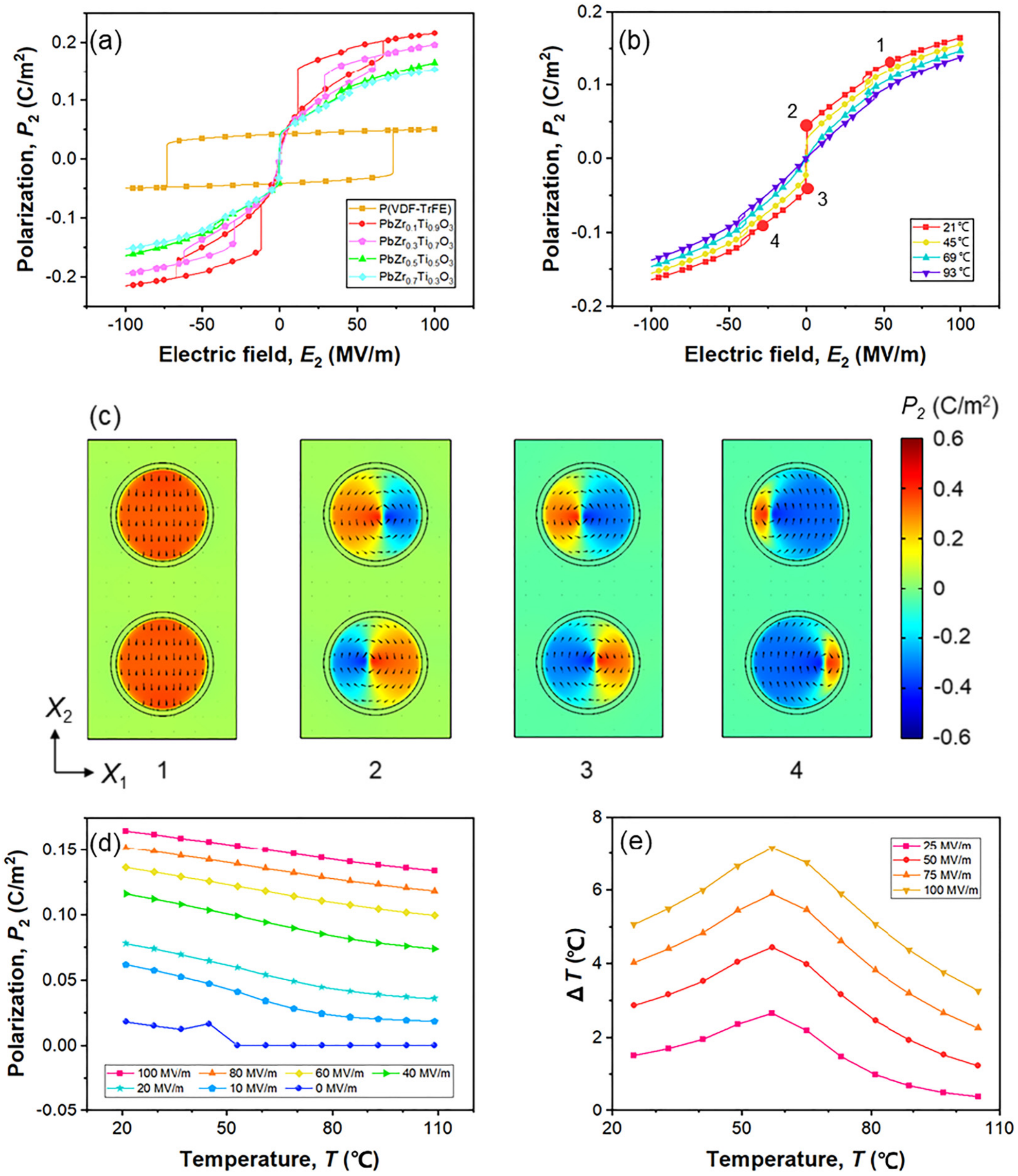

FIG. 5. (a) Comparison of P–E loops at 21 °C of the P(VDF-TrFE) matrix and ferroelectric nanocomposites filled with different PZT nanoparticles of several component x. (b) P–E loops at different temperatures of the ferroelectric nanocomposite P(VDF-TrFE)–$PZT_{0.5}$. (c) Representative domain structures corresponding to the points in (b) to explain the emergence of hysteresis-free loop at 21 °C. (d) P–T curves at different electric fields, and (e) ΔT–T curves under several electric field changes of the ferroelectric nanocomposite P(VDF-TrFE)–$PZT_{0.5}$.

gradually declines. It is noticed that when the component x is further decreased to 0.5, both the double loop behavior and the hysteresis phenomenon of the P–E loops almost disappear.

The ferroelectric nanocomposite filled with nanoparticles of $PbZr_{0.5}Ti_{0.5}O_3$ [P(VDF-TrFE)–$PZT_{0.5}$] is then selected as another instance to explain the effect of component x. The P–E loop of P(VDF-TrFE)–$PZT_{0.5}$ at 21 °C is given in Fig. 5(b) to capture a clear view of shape changing. Several characteristic points are picked out along the P–E loop to demonstrate microscopic mechanism from the aspect of domain evolution, and the corresponding domain structures are presented in Fig. 5(c). Upon unloading of electric field from the maximum value, the domain transition from single domain to vortex domain is also observed in the $PZT_{0.5}$ particle from points 1 to 2. Differing from the case of P(VDF-TrFE)–

27 November 2025 08:52:18

© Author(s) 2024

$PZT_{0.9}$, the vortex domain obtained in the P(VDF-TrFE)–$PZT_{0.5}$ is rotated an angle in plane of X_1–X_2 and the transition process is more sedate due to the decreasing of tetragonality when the component x is approaching to the morphotropic phase boundary (MPB). The emergence of negative domains within the PZT nanoparticle-filled region from points 1 to 2 reduces the overall average polarization. Transitioning from point 2 to point 3, the electric field is reduced from a positive value down to zero and then increased in the negative direction. Concurrently, in the PZT nanoparticle-filled region, the area of negatively polarized domains grows, causing the overall average polarization shifted from positive to negative. During this stage, the direction of polarization within the P(VDF-TrFE) matrix is also switched by the domain inside the PZT nanoparticle. Continue to intensify the electric field along the $-X_2$ direction from points 3 to 4, the negative domain areas within the PZT nanoparticle-filled regions expand, further elevating the magnitude of the overall average polarization. The temperature-dependent P–E loops of ferroelectric nanocomposite P(VDF-TrFE)–$PZT_{0.5}$ are summarized in Fig. 5(b). The data reveal that an increase in temperature tends to simultaneously weaken the polarization of the P(VDF-TrFE)–$PZT_{0.5}$ at each electric field state. Figure 5(d) present the P–T curves of the P(VDF-TrFE)–$PZT_{0.5}$ under different electric fields to display the temperature influence on polarization. Expect for the slight drop existed at the remnant polarization state with temperature rising, all the P–T curves show similar behavior to that of P(VDF-TrFE) but with decreased decline rate of polarization. In the absence of electric field, as temperature increase from 37 to 45 °C, more polarization vectors in the P(VDF-TrFE) matrix region are switched to align along the $+X_2$ direction, while no significant change of polarization vectors are observed in the PZT nanoparticle-filled regions, resulting in an increase in the overall average polarization of P(VDF-TrFE)–$PZT_{0.5}$. ΔT–T curves of the P(VDF-TrFE)–$PZT_{0.5}$ are illustrated in Fig. 5(e), and the ΔT also reaches the peak around 57 °C. Specifically, the $\Delta T_{\max}$ of P(VDF-TrFE)–$PZT_{0.5}$ is 4.44 °C when an electric field of 50 MV/m is applied and reaches 7.15 °C under 100 MV/m.

Figures 6(a) and 6(b) provide a comparison for the ΔT–T curves of P(VDF-TrFE)–$PZT_{0.9}$, P(VDF-TrFE)–$PZT_{0.5}$ and P(VDF-TrFE) under electric field changes of 50 and 100 MV/m, respectively. From Fig. 6(a), it is evident that under the same electric field of 50 MV/m, the P(VDF-TrFE)–$PZT_{0.9}$ owns better ECE compared with P(VDF-TrFE), which is mainly reflected by the

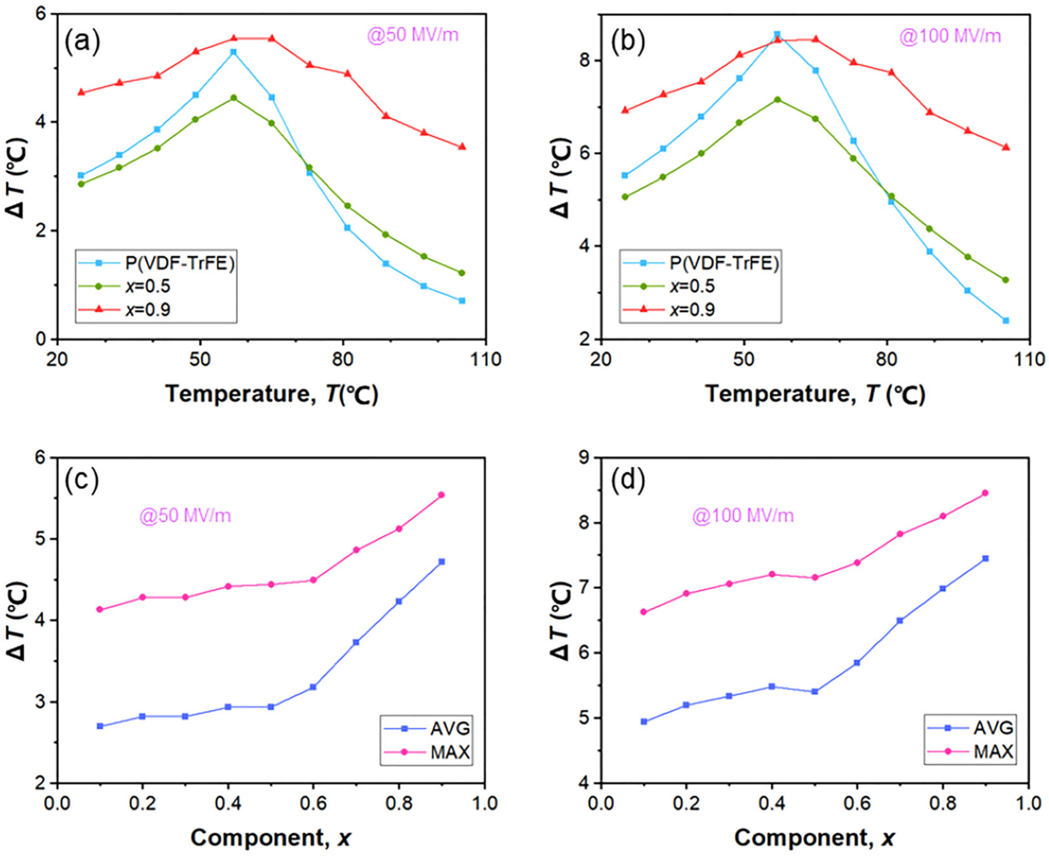

FIG. 6. Comparison of ΔT–T curves of the P(VDF-TrFE) matrix and ferroelectric nanocomposites filled with different PZT nanoparticles of several component x under the electric field of (a) 50 and (b) 100 MV/m. The relationship between the ATC ΔT and component x under the electric field of (c) 50 and (d) 100 MV/m, where MAX represents the maximum value and AVG represents the average value in the whole temperature range.

27 November 2025 08:52:18

© Author(s) 2024

larger ΔT and wider working temperature range. Although the P(VDF-TrFE)–PZT$_{0.5}$ displays an inferior value of ΔT at lower temperature, it also possesses a broadened working temperature range. Figure 6(b) reveals that the P(VDF-TrFE)–PZT$_{0.9}$ also maintains relatively superior ECE at a higher electric field change. The average ΔT (i.e., ΔT_{avg}) within the temperature range (21 and 93 °C) is calculated to serve as a metric to more concretely demonstrate the ECE of the ferroelectric nanocomposites over a broader operation temperature range. Figures 6(c) and 6(d) exhibit the curves of ΔT_{avg} and ΔT_{max} vs the component x under 50 and 100 MV/m electric fields, respectively. When the component x is larger than the MPB concentration (i.e., $x > 0.5$), both ΔT_{max} and ΔT_{avg} are improved rapidly with x increasing. The presence of filled PZT nanoparticles significantly influences the ECE of the ferroelectric nanocomposites. It is also indicated that the optimal ECE, characterized by the highest ΔT_{max} and ΔT_{avg}, is achieved at $x = 0.9$ within the computed range. The results suggest that the ferroelectric nanocomposite, particularly the P(VDF-TrFE)–PZT$_{0.9}$ formulation introduced in this study, is able to exhibit better ECE performance than that of P(VDF-TrFE). Additionally, it offers an extended temperature range of operation near room temperature. The finding in this work is crucial for the ECE regulation of the ferroelectric nanocomposites by optimizing the component of filled nanoparticles.

IV. CONCLUSION

In summary, based on the thermodynamic theory of ferroelectric materials, the phase-field method is used to study the ECE behavior of ferroelectric nanocomposites consisting of the P(VDF-TrFE) matrix and PZT nanoparticles. It is found that the introduction of nanoparticles has a large influence on the microscopic domain structure of the entire system. Electric field induced domain transition from single domain to polar vortex is observed in nanocomposite P(VDF-TrFE)–PZT$_{0.9}$, resulting in a double hysteresis loop. On this basis, the indirect method based on the Maxwell relation is employed to calculate the temperature-dependent ATC values. Benefited from the domain transition with the increase of temperature under several electric fields, enhanced ECE with a large working temperature region near room temperature is achieved through the carefully designed ferroelectric nanocomposite P(VDF-TrFE)–PZT$_{0.9}$. Finally, the ΔT–T curves generate a peak of $\Delta T_{\mathrm{max}} = 5.54$ °C at 50 MV/m and $\Delta T_{\mathrm{max}} = 8.43$ °C at 100 MV/m. The influence of the nanofiller particle component x on the ECE of ferroelectric nanocomposites is further investigated. The maximum ATC of ΔT_{max} and the average ATC of ΔT_{avg} are obtained for ferroelectric nanocomposites in the range of x from 0.1 to 0.9. When the component x is larger than the MPB, both the ΔT_{max} and ΔT_{avg} are enhanced sharply with the x increases continuously. The main results of the present work show that the ECE of ferroelectric nanocomposites can be effectively improved by the introduction of nanoparticles and then further regulated via changing the component x of filled nanoparticle. The simulation results suggest an effective way to tune the ECE of ferroelectric nanocomposites through the design of domain transitions and provide a new theoretical and practical guidance for the development of ECE coolers based on ferroelectric nanocomposites, which can be used in novel application like flexible wearable refrigeration.

ACKNOWLEDGMENTS

This work was financially supported by the National Natural Science Foundation of China (NNSFC) (Grant Nos. 12272338 and 12192214). The work described in this paper was partially supported by a fellowship award from the Research Grants Council of the Hong Kong Special Administrative Region, China (Project No. PolyU PDFS2223-5S08). X. Hou also would like to acknowledge support from the PolyU Distinguished Postdoctoral Fellowship Scheme (No. 1-YWBC), and the PolyU grant (G-UAMV).

AUTHOR DECLARATIONS

Conflict of Interest

The authors have no conflicts to disclose.

Author Contributions

Zeqing Yu: Conceptualization (equal); Data curation (equal); Formal analysis (equal); Investigation (equal); Methodology (equal); Software (equal); Visualization (equal); Writing – original draft (equal); Writing – review & editing (equal). **Xu Hou:** Conceptualization (equal); Data curation (equal); Formal analysis (equal); Funding acquisition (equal); Investigation (equal); Methodology (equal); Software (equal); Supervision (equal); Validation (equal); Visualization (equal); Writing – original draft (equal); Writing – review & editing (equal). **Sizheng Zheng:** Software (equal); Validation (equal); Writing – review & editing (equal). **Chengwen Bin:** Resources (equal); Validation (supporting); Writing – review & editing (equal). **Jie Wang:** Conceptualization (equal); Formal analysis (equal); Funding acquisition (lead); Methodology (equal); Project administration (lead); Resources (lead); Software (equal); Supervision (lead); Validation (equal); Visualization (equal); Writing – review & editing (equal).

27 November 2025 08:52:18

DATA AVAILABILITY

The data that support the findings of this study are available from the corresponding author upon reasonable request.

APPENDIX: MATERIAL PARAMETERS ULTILIZED IN THIS WORK

Table I indicates the material parameters of P(VDF-TrFE). Tables II and III indicate the material parameters of PZT$_{0.9}$ and PZT$_{0.5}$, respectively.

TABLE I. The material parameters of the P(VDF-TrFE).

Landau energy coefficient	Electrostriction coefficient
$\alpha_1 = 5.9(\mathrm{T} - 332.26) \times 10^7\ \mathrm{C^{-2}\ m^2\ N}$	$Q_{11} = -0.0162\ \mathrm{C^{-2}\ m^4}$
$\alpha_{11} = 6.378 \times 10^{11}\ \mathrm{C^{-4}\ m^6\ N}$	$Q_{12} = 0.0441\ \mathrm{C^{-2}\ m^4}$
$\alpha_{12} = 1.276 \times 10^{12}\ \mathrm{C^{-4}\ m^6\ N}$	$Q_{44} = -0.12\ \mathrm{C^{-2}\ m^4}$
$\alpha_{111} = 1.851 \times 10^{12}\ \mathrm{C^{-6}\ m^{10}\ N}$	Gradient coefficient
$\alpha_{112} = 5.554 \times 10^{12}\ \mathrm{C^{-6}\ m^{10}\ N}$	$G_{11}/G_{110} = 0.5$
$\alpha_{123} = 1.111 \times 10^{13}\ \mathrm{C^{-6}\ m^{10}\ N}$	$G_{12}/G_{110} = 0.0$
Elastic constant	$G_{44}/G_{110} = 0.5$
$C_{11} = 4.88 \times 10^{10}\ \mathrm{N\ m^{-2}}$	$G_{110} = 2.021 \times 10^{-9}\ \mathrm{C^{-2}\ m^4\ N}$
$C_{12} = 5.6 \times 10^{9}\ \mathrm{N\ m^{-2}}$	Relative dielectric constant
$C_{44} = 2.16 \times 10^{10}\ \mathrm{N\ m^{-2}}$	$\varepsilon_r = 200$

© Author(s) 2024

TABLE II. The material parameters of the $\text{PZT}_{0.9}$.

Landau energy coefficient	Electrostriction coefficient
$\alpha_1 = 3.65(\mathrm{T} - 740.77) \times 10^5\ \mathrm{C}^{-2}\ \mathrm{m}^2\ \mathrm{N}$	$Q_{11} = 0.0850\mathrm{C}^{-2}\ \mathrm{m}^4$
$\alpha_{11} = -5.845 \times 10^7\ \mathrm{C}^{-4}\ \mathrm{m}^6\ \mathrm{N}$	$Q_{12} = -0.0235\mathrm{C}^{-2}\ \mathrm{m}^4$
$\alpha_{12} = 7.063 \times 10^8\ \mathrm{C}^{-4}\ \mathrm{m}^6\ \mathrm{N}$	$Q_{44} = 0.0657\mathrm{C}^{-2}\ \mathrm{m}^4$
$\alpha_{111} = 2.518 \times 10^8\ \mathrm{C}^{-6}\ \mathrm{m}^{10}\ \mathrm{N}$	Gradient coefficient
$\alpha_{112} = 8.099 \times 10^8\ \mathrm{C}^{-6}\ \mathrm{m}^{10}\ \mathrm{N}$	$G_{11}/G_{110} = 0.6$
$\alpha_{123} = -4.359 \times 10^9\ \mathrm{C}^{-6}\ \mathrm{m}^{10}\ \mathrm{N}$	$G_{12}/G_{110} = 0.0$
Elastic constant	$G_{44}/G_{110} = 0.6$
$C_{11} = 1.7042 \times\ 10^{11}\ \mathrm{N\ m}^{-2}$	$G_{110} = 1.617 \times 10^{-10}\ \mathrm{C}^{-2}\ \mathrm{m}^4\ \mathrm{N}$
$C_{12} = 7.608 \times\ 10^{10}\ \mathrm{N\ m}^{-2}$	Relative dielectric constant
$C_{44} = 8.3333 \times\ 10^{10}\ \mathrm{N\ m}^{-2}$	$\varepsilon_r = 100$

TABLE III. The material parameters of the $\text{PZT}_{0.5}$.

Landau energy coefficient	Electrostriction coefficient
$\alpha_1 = 1.33(\mathrm{T} - 665.57) \times 10^5\ \mathrm{C}^{-2}\ \mathrm{m}^2\ \mathrm{N}$	$Q_{11} = 0.0966\ \mathrm{C}^{-2}\ \mathrm{m}^4$
$\alpha_{11} = 4.764 \times 10^7\ \mathrm{C}^{-4}\ \mathrm{m}^6\ \mathrm{N}$	$Q_{12} = 0.0071\ \mathrm{C}^{-2}\ \mathrm{m}^4$
$\alpha_{12} = 1.735 \times 10^8\ \mathrm{C}^{-4}\ \mathrm{m}^6\ \mathrm{N}$	$Q_{44} = 0.0819\ \mathrm{C}^{-2}\ \mathrm{m}^4$
$\alpha_{111} = 1.336 \times 10^8\ \mathrm{C}^{-6}\ \mathrm{m}^{10}\ \mathrm{N}$	Gradient coefficient
$\alpha_{112} = 6.128 \times 10^8\ \mathrm{C}^{-6}\ \mathrm{m}^{10}\ \mathrm{N}$	$G_{11}/G_{110} = 0.6$
$\alpha_{123} = -2.894 \times 10^9\ \mathrm{C}^{-6}\ \mathrm{m}^{10}\ \mathrm{N}$	$G_{12}/G_{110} = 0.0$
Elastic constant	$G_{44}/G_{110} = 0.6$
$C_{11} = 1.545 \times\ 10^{11}\ \mathrm{N\ m}^{-2}$	$G_{110} = 1.617 \times 10^{-10}\ \mathrm{C}^{-2}\ \mathrm{m}^4\ \mathrm{N}$
$C_{12} = 8.405 \times\ 10^{10}\ \mathrm{N\ m}^{-2}$	Relative dielectric constant
$C_{44} = 3.484 \times\ 10^{10}\ \mathrm{N\ m}^{-2}$	$\varepsilon_r = 100$

REFERENCES

[1] G. J. M. Velders, D. W. Fahey, J. S. Daniel, M. McFarland, and S. O. Andersen, Proc. Natl. Acad. Sci. U.S.A. **106**(27), 10949–10954 (2009).

[2] R. van Erp, R. Soleimanzadeh, L. Nela, G. Kampitsis, and E. Matioli, Nature **585**(7824), 211–216 (2020).

[3] R. J. Ma, Z. Y. Zhang, K. W. Tong, D. Huber, R. Kornbluh, Y. S. Ju, and Q. B. Pei, Science **357**(6356), 1130–1134 (2017).

[4] X. Qian, X. Chen, L. Zhu, and Q. M. Zhang, Science **380**(6645), eadg0902 (2023).

[5] J. Y. Shi, D. L. Han, Z. C. Li, L. Yang, S. G. Lu, Z. F. Zhong, J. P. Chen, Q. M. Zhang, and X. S. Qian, Joule **3**(5), 1200–1225 (2019).

[6] W. Thomson, London Edinburgh Dublin Phil. Mag. J. Sci. **5**(28), 4–27 (1878).

[7] P. Kobeko and J. Kurtschatov, Z. Phys. **66**, 192–205 (1930).

[8] J. Shi, D. Han, Z. Li, L. Yang, S.-G. Lu, Z. Zhong, J. Chen, Q. M. Zhang, and X. Qian, Joule **3**(5), 1200–1225 (2019).

[9] C. Bin, X. Hou, Z. Yu, L. Liao, H. Yang, Y. Liu, and J. Wang, ACS Appl. Mater. Interfaces **16**(2), 2231–2239 (2024).

[10] X. Moya, S. Kar-Narayan, and N. D. Mathur, Nat. Mater. **13**(5), 439–450 (2014).

[11] P. M. Margosian, *Parametric Study of a Thermoelectrostatic Generator for Space Applications* (National Aeronautics and Space Administration, 1965).

[12] B. T. Matthias, J. Appl. Phys. **38**(3), 928–930 (1967).

[13] T. Mitsui, I. Tatsuzaki, E. Nakamura, and Y. Ishibashi, *An Introduction to the Physics of Ferroelectrics* (Gordon and Breach Science Publishers, NY, 1976).

[14] J. F. Scott, F. M. Ross, C. A. P. de Araujo, M. C. Scott, and M. Huffman, MRS Bull. **21**(7), 33–39 (1996).

[15] A. S. Mischenko, Q. Zhang, J. F. Scott, R. W. Whatmore, and N. D. Mathur, Science **311**(5765), 1270–1271 (2006).

[16] Y. Liu, J. Wei, P. E. Janolin, I. C. Infante, J. Kreisel, X. Lou, and B. Dkhil, Phys. Rev. B **90**(10), 104107 (2014).

[17] G. Akcay, S. P. Alpay, G. A. Rossetti, Jr., and J. F. Scott, J. Appl. Phys. **103**(2) (2008).

[18] Y. B. Ma, A. Grünebohm, K.-C. Meyer, K. Albe, and B.-X. Xu, Phys. Rev. B **94**, 094113 (2016).

[19] B. Neese, B. J. Chu, S. G. Lu, Y. Wang, E. Furman, and Q. M. Zhang, Science **321**(5890), 821–823 (2008).

[20] G. Z. Zhang, B. Y. Fan, P. Zhao, Z. Y. Hu, Y. Liu, F. H. Liu, S. L. Jiang, S. L. Zhang, H. L. Li, and Q. Wang, ACS Appl. Energy Mater. **1**(3), 1344–1354 (2018).

[21] M. Tokkan, M. M. Demir, and U. Adem, Ceram. Int. **49**(2), 2904–2910 (2023).

[22] G. Z. Zhang, X. S. Zhang, T. N. Yang, Q. Li, L. Q. Chen, S. L. Jiang, and Q. Wang, ACS Nano **9**(7), 7164–7174 (2015).

[23] Q. Li, G. Zhang, X. Zhang, S. Jiang, Y. Zeng, and Q. Wang, Adv. Mater. **27**(13), 2236–2241 (2015).

[24] T. Kawai and K.-I. Kakimoto, Mater. Lett. **301**, 130277 (2021).

[25] K. Zou, C. Shao, P. Bai, C. Zhang, Y. Yang, R. Guo, H. Huang, W. Luo, R. Ma, Y. Cao, A. Sun, G. Zhang, and S. Jiang, Nano Lett. **22**(16), 6560–6566 (2022).

[26] J. Wang, M. Liu, Y. Zhang, T. Shimada, S. Q. Shi, and T. Kitamura, J. App. Phys. **115**(16), 164102 (2014).

[27] B. Peng, H. Fan, and Q. Zhang, Adv. Funct. Mater. **23**(23), 2987–2992 (2013).

[28] X. Hou, H. Li, T. Shimada, T. Kitamura, and J. Wang, J. Appl. Phys. **123**(12), 124103 (2018).

[29] H. H. Wu, J. Zhu, and T. Y. Zhang, Nano Energy **16**, 419–427 (2015).

[30] J. Zhu, H. Chen, X. Hou, L. Xu, H. Wu, and J. Wang, J. Appl. Phys. **125**(23), 234101 (2019).

[31] Y. U. Wang, J. Mater. Sci. **44**(19), 5225–5234 (2009).

[32] M. Guo, C. Guo, J. Han, S. Chen, S. He, T. Tang, Q. Li, J. Strzalka, J. Ma, D. Yi, K. Wang, B. Xu, P. Gao, H. Huang, L.-Q. Chen, S. Zhang, Y.-H. Lin, C.-W. Nan, and Y. Shen, Science **371**(6533), 1050–1056 (2021).

[33] M. Guo, E. Xu, H. Huang, C. Guo, H. Chen, S. Chen, S. He, L. Zhou, J. Ma, Z. Shen, B. Xu, D. Yi, P. Gao, C.-W. Nan, N. D. Mathur, and Y. Shen, Nat. Commun. **15**(1), 348 (2024).

[34] G. Tian, W. Deng, T. Yang, D. Xiong, H. Zhang, B. Lan, L. Deng, B. Zhang, L. Jin, H. Huang, Y. Sun, S. Wang, and W. Yang, Small **19**(16), 2207947 (2023).

[35] J. Wang, W. Shu, T. Shimada, T. Kitamura, and T. Y. Zhang, Acta Mater. **61**(16), 6037–6049 (2013).

[36] T. J. Lewis, J. Phys. D: Appl. Phys. **38**(2), 202–212 (2005).

[37] S. Zheng, F. Du, L. Zheng, D. Han, Q. Li, J. Shi, J. Chen, X. Shi, H. Huang, Y. Luo, Y. Yang, P. O'Reilly, L. Wei, N. de Souza, L. Hong, and X. Qian, Science **382**(6674), 1020–1026 (2023).

[38] J.-F. Du, J.-H. Zhao, and J. Ren, J. Fuel Chem. Technol. **49**(7), 986–996 (2021).

[39] Y. Liu, H. Aziguli, B. Zhang, W. Xu, W. Lu, J. Bernholc, and Q. Wang, Nature **562**(7725), 96–100 (2018).

[40] Y. Liu, A. Haibibu, W. Xu, Z. Han, and Q. Wang, Adv. Funct. Mater. **30**(25), 2000648 (2020).

[41] K. M. Rabe, C. H. Ahn, and J.-M. Triscone, *Physics of Ferroelectrics: A Modern Perspective* (Springer Science & Business Media, 2007).

[42] R. B. Olsen, W. F. Butler, D. A. Payne, B. A. Tuttle, and P. C. Held, Phys. Rev. Lett. **45**(17), 1436–1438 (1980).

[43] J. Li, J. Li, S. Qin, X. Su, L. Qiao, Y. Wang, T. Lookman, and Y. Bai, Phys. Rev. Appl. **11**(4), 044032 (2019).

[44] M. E. Lines and A. M. Glass, *Principles and Applications of Ferroelectrics and Related Materials* (Oxford University Press, 2001).

[45] P. D. Thacher, J. Appl. Phys. **39**(4), 1996–2002 (2003).

[46] A. N. Morozovska, E. A. Eliseev, M. D. Glinchuk, H. V. Shevliakova, G. S. Svechnikov, M. V. Silibin, A. V. Sysa, A. D. Yaremkevich, N. V. Morozovsky, and V. V. Shvartsman, Phys. Rev. Materials **3**(10), 104414 (2019).

[47] S. G. Lu, B. Rozic, Z. Kutnjiak, and Q. M. Zhang, Integr. Ferroelectr. **125**(1), 176–185 (2011).

[48] Y. Liu, A. Haibibu, W. Xu, Z. Han, and Q. Wang, Adv. Funct. Mater. **30**(25), 2000648 (2020).

27 November 2025 08:52:18

© Author(s) 2024